Fluxional Bonds in Tubular Molecular Rotors B_3-[Ta@B_{18}] and B_4-[Ta@B_{18}]$^+$ in 18-Electron Configurations

Hai-Ru Li[1] · Min Zhang[1] · Miao Yan[1] · Wen-Yan Zan[1] · Xin-Xin Tian[1] · Yue-Wen Mu[1] · Si-Dian Li[1]

Abstract

Boron and metal-doped boron nanoclusters possess unique fluxional behaviors in dynamics. Detailed bonding analyses performed in this work indicate that, similar to the experimentally observed B_2-[Ta@B_{18}]$^-$ (**1**), the theoretically predicted tubular molecular rotors B_3-[Ta@B_{18}] (**2**) and B_4-[Ta@B_{18}]$^+$ (**3**) possess typical fluxional 4c–2e and 3c–2e σ-bonds atop the Ta-centered [Ta@B_{18}] double-ring tube between the B_n unit (n = 3, 4) and upper B_9 ring, unveiling the fluxional bonding nature of the B_n-[Ta@B_{18}]^q complex series (n = 2–4, q = n − 3) which follow the 18-electron rule in different charge states. Chiral conversions via pseudo-rotations are observed in the fluxional processes between the B_n unit (n = 3, 4) and Ta-centered [Ta@B_{18}] double-ring tube.

Keywords First-principles theory · Geometrical structures · Electronic structures · Fluxional bonds · Molecular rotors

Introduction

As prototypical electron-deficient element, the chemistry of boron is dominated by multicenter-two-electron bonds (mc–2e bonds) in both bulk allotropes and polyhedral molecules [1]. Over the past 2 decades, persistent joint photoelectron spectroscopy (PES) and theoretical investigations have unveiled a rich landscape for small monoanionic boron clusters from planar or quasi-planar B_n^- (n = 3–38) to cage-like B_n^- (n = 39, 40) which are all characterized with delocalized mc–2e σ and π bonds [2–9]. Recent theoretical investigations extend the all-boron fullerenes into a B_n^q borospherene family (n = 36–42, q = n − 40) which are composed of twelve interwoven double chains in the universal bonding pattern of σ + π double delocalization [10–13]. Ion-mobility measurements, on the other hand, show that B_n^+ monocations possess double-ring (DR) tubular structures in the size range

between n = 16–25, revealing another important structural domain in boron nanoclusters [14, 15].

It has been established in both experiments and theory that transition-metal doping leads to an early planar-to-tubular structural transition in small boron monoanions. The first perfect transition-metal-centered DR tubular Co@B_{16}^- was observed in 2015 [16]. Drum-like MnB$_{16}^-$ [17], RhB$_{18}^-$ [18], and Ta@B_{20}^- [19] were later experimentally confirmed, with the Ta-centered DR tubular C_s B_2-[Ta@B_{18}]$^-$ (1) as the global minimum (GM) of TaB$_{20}^-$ possessing the highest coordination number of CN_{max} = 20 known in experiments to date. The viable possibility of Ta-centered DR tubular C_s B_3-[Ta@B_{18}] (2) and C_{3v} B_4-[Ta@B_{18}]$^+$ (3) with even higher coordination numbers of CN = 21 and 22, respectively, have also been predicted recently as the well defined GMs of the systems at first-principles theory level, based on extensive global searches [20]. These tubular molecular rotors in 18-electron configurations all turn out to exhibit fluxional behaviors in molecular dynamic simulations at finite temperatures and may serve as interesting species to be targeted in future experiments.

In three recent consecutive papers [21–23] our group predicted the existence of fluxional bonds (FBs) in planar C_{2v} B_{19}^-, tubular C_s B_2-[Ta@B_{18}]$^-$ (1), cage-like C_3/C_2 B_{39}^-, and half-sandwich C_s MB$_{18}^-$ (M = K, Rb, and Cs) and NiB$_{11}^-$, unveiling the bonding nature of these fluxional

✉ Si-Dian Li
lisidian@sxu.edu.cn

[1] Institute of Molecular Science, Shanxi University, Taiyuan 030006, China

boron nanoclusters. Similar FBs also exist in planar C_{2v} B_{11}^- ($B_2@B_9^-$) [24], C_{2v} B_{13}^+($B_3@B_{10}^+$) [15, 25], and C_{2v} B_{15}^+ ($B_4@B_{11}^+$) [26, 27]. Fluxional bonds in these nanoclusters form and break constantly in concerted mechanisms under certain conditions. As a continuation in this direction, in this work, we present a detailed bonding analysis on C_s B_3-[Ta@B$_{18}$] (**2**) and C_{3v} B_4-[Ta@B$_{18}$]$^+$ (**3**) to describe the delocalized FBs in these DR tubular species which have more sophisticated and interesting potential energy surfaces than the previously reported B_2-[Ta@B$_{18}$]$^-$ (**1**). Chiral conversions exist in the pseudo-rotation processes between the B_n unit (n = 3, 4) and [Ta@B$_{18}$] double-ring tube. We aim to unveil the fluxional bonding nature of the B_n-[Ta@B$_{18}$]^q complex series (n = 2–4, q = n − 3) which follow the 18-electron rule in different charge states.

Theoretical Procedure

The GMs and transition states (TS) of B_3-[Ta@B$_{18}$] and B_4-[Ta@B$_{18}$]$^+$ were fully optimized at the hybrid DFT-PBE0 [28] level using the Gaussian 09 package [29], with the basis set of 6-311+G(d) [30] for boron and Stuttgart relativistic small-core pseudopotential for Ta [31, 32]. Special attention was paid to locate the transition states of B_4-[Ta@B$_{18}$]$^+$ (**3**) which turns out to have a much more complicated potential energy surface than both B_2-[Ta@B$_{18}$]$^-$ (**1**) and C_s B_3-[Ta@B$_{18}$] (**2**). Frequency checks were performed to make sure all the optimized structures are true minima or transition states on the potential energy surfaces of the systems. Both forward and backward reaction paths were followed by integrating the intrinsic reaction coordinates of Ta@B$_{21}$ and Ta@B$_{22}^+$. Detailed bonding analyses were performed on the GMs, TSs, and intermediate states of the concerned species using the adaptive natural density portioning (AdNDP) approach [33] which recovers both the localized and delocalized bonds in the concerned systems. AdNDP has proven to be reliable in analyzing the bonding patterns of various boron and boron-based nanoclusters [2–9, 21–23].

Results and Discussion

Structures and Stabilities

The GM structures of TaB$_{20}^-$, TaB$_{21}$, and TaB$_{22}^+$ are comparatively shown Fig. 1, with their intermediate states and transition states on the potential surfaces collectively depicted in Fig. 2. The GMs of C_s B_3-[Ta@B$_{18}$] (**2**) and C_{3v} B_4-[Ta@B$_{18}$]$^+$ (**3**) follow the same structural pattern as the experimentally observed C_s B_2-[Ta@B$_{18}$]$^-$ (**1**) [19],
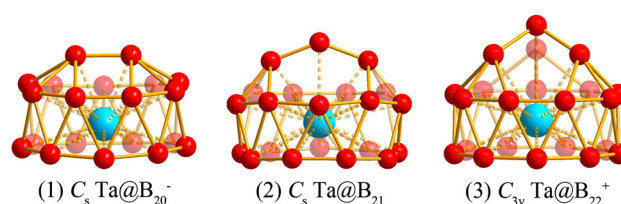
Fig. 1 Optimized GM structures of B_2-[Ta@B$_{18}$]$^-$ (1), B_3-[Ta@B$_{18}$] (2) and B_4-[Ta@B$_{18}$]$^+$ (3) at PBE0 level, with their point-group symmetries of C_s, C_s, and C_{3v} indicated in italic, respectively
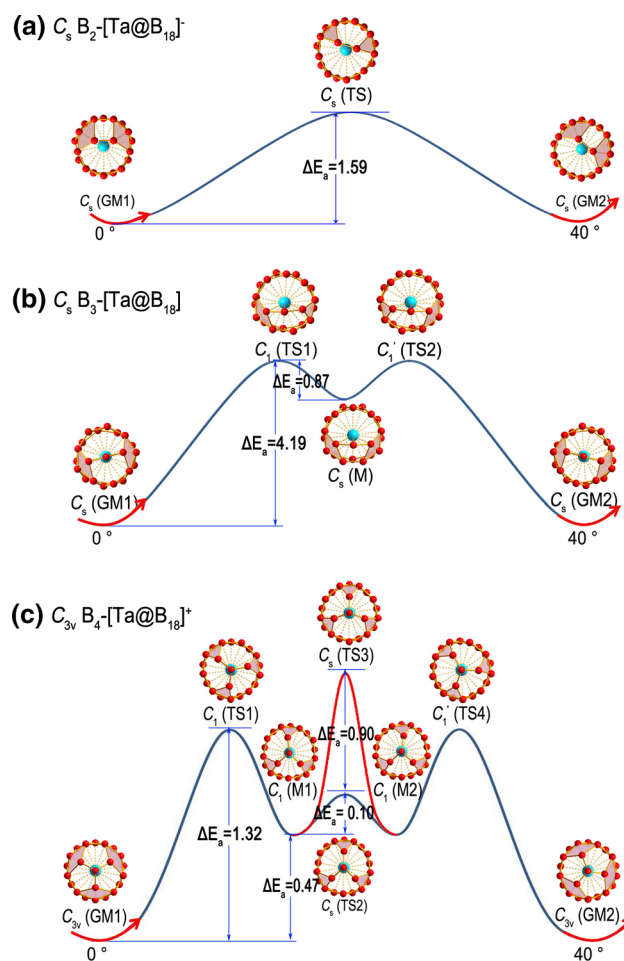
Fig. 2 Intermediate states and transition states of **a** B_2-[Ta@B$_{18}$]$^-$ (1) **b** B_3-[Ta@B$_{18}$] (2), and **c** B_4-[Ta@B$_{18}$]$^+$ (3) in the rotational angle of 40° in one step, with energies relative to their global minima indicated in kcal/mol at PBE0 level. The fluxional 4c–2e and 3c–2e σ bonds are highlighted in pink (Color figure online)

with a V-shaped B_3 chain ($\equiv$B–B–B$\equiv$) and a B_4 tetrahedron atop a Ta-centered Ta@B$_{18}$ DR tube, respectively (Fig. 1). Extensive molecular dynamics simulations indicate that the B_n units in B_n-[Ta@B$_{18}$]^q complexes (n = 2, 3, 4, q = 3 − n) rotate around the molecular axis almost freely in concerted mechanisms with respect to the [Ta@B$_{18}$] DR tube in B_2-[Ta@B$_{18}$]$^-$ (**1**), B_3-[Ta@B$_{18}$] (**2**), and B_4-[Ta@B$_{18}$]$^+$ (**3**) at 300, 400, and 300 K,

respectively (Videos S1, S2, and S3 in ESI). One intermediate state C_s B$_3$-[Ta@B$_{18}$] (M) ($\equiv$B–B–B$\equiv$) with the relative energy of ΔE_a = 3.32 kcal/mol and two degenerate chiral transition states C_1 B$_3$-[Ta@B$_{18}$] (TS1) (=B–B–B$\equiv$) and C_1' B$_3$-[Ta@B$_{18}$] (TS2) ($\equiv$B–B–B=) with ΔE_{a-} = 4.19 kcal/mol are located on the potential energy surface of neutral B$_3$-[Ta@B$_{18}$] (Fig. 2b). The energy barrier of ΔE_a = 0.87 kcal/mol from the intermediate state (M) to either TS1 or TS2 is not overwhelming, which, as shown in Video S2, can be overcome by thermo-excitations at 400 K. There exists a pseudo-rotation between the B$_3$ unit and the DR [Ta@B$_{18}$] tube in B$_3$-[Ta@B$_{18}$] (2) with the rotational angle of 40° in each step. A chiral conversion via pseudo-rotation is observed on the pathway between the two degenerate enantiomers TS1 and TS2 in B$_3$-[Ta@B$_{18}$] (2). B$_3$-[Ta@B$_{18}$] (2) therefore possesses a more complicated potential energy surface than that of the previously reported B$_2$-[Ta@B$_{18}$]$^-$ (1) (Fig. 2a) [19, 21]. The C_s (GM1) $\rightarrow$ C_1 (TS1) $\rightarrow$ C_s (M) $\rightarrow$ C_1' (TS2) $\rightarrow$ C_s (GM2) fluxional process repeats itself nine times in a full circle of the pseudo-rotation, similar to the situation observed in B$_2$-[Ta@B$_{18}$]$^-$ (1) [21].

B$_4$-[Ta@B$_{18}$]$^+$ (3) turns out to have a more complicated potential energy surface (Fig. 2c) than that of B$_3$-[Ta@B$_{18}$] (2) (Fig. 2b). Two degenerate chiral transition states C_1 B$_4$-[Ta@B$_{18}$]$^+$ (TS1) and C_1' B$_4$-[Ta@B$_{18}$]$^+$ (TS4) with ΔE_a = 1.32 kcal/mol, two degenerate chiral intermediate states C_1 B$_4$-[Ta@B$_{18}$]$^+$ (M1) and C_1' B$_4$-[Ta@B$_{18}$]$^+$ (M2) with ΔE_a = 0.47 kcal/mol, one low-lying transition state C_s B$_4$-[Ta@B$_{18}$]$^+$ (TS2) with ΔE_a = 0.57 kcal/mol, and one high-lying transition state C_s B$_4$-[Ta@B$_{18}$]$^+$ (TS3) with ΔE = 1.47 kcal/mol are identified on the potential energy surface of B$_4$-[Ta@B$_{18}$]$^+$ (3) (Fig. 2c). It has much lower energy barriers (0.1–1.32 kcal/mol) than that (4.19 kcal/mol) of B$_3$-[Ta@B$_{18}$] (2). Chiral conversions exist between both the two degenerate transition states TS1 and TS4 and two degenerate intermediate states M1 and M2. The rate-determinant step possesses an energy barrier of 1.32 kcal/mol which is slightly lower than that (1.59 kcal/mol) of the experimentally observed B$_2$-[Ta@B$_{18}$]$^-$ (1) at PBE0 level. The two transition states C_s TS2 and C_s TS3 which can be transformed from one to the other via a slight buckling in the B$_6$ rings on the top perpendicular to the molecular mirror plane possess a large reaction rate ratio of k$_2$/k$_3$ = 2.5, indicating that the C_1 M1—C_s TS2—C_1' M2 chiral conversion plays a dominant role (72%) in the fluxional process. The high-symmetry C_{3v} B$_4$ tetrahedron in B$_4$-[Ta@B$_{18}$]$^+$ (3) rotates almost freely atop the Ta-centered [Ta@B$_{18}$] tube during molecular dynamics simulations at 300 K (Video S3), with the rotational angle of 40° in each step, similar to both C_s B$_2$-[Ta@B$_{18}$]$^-$ (1) (Video S1) and C_s B$_3$-[Ta@B$_{18}$] (2) (Video S2). The GM of B$_4$-[Ta@B$_{18}$]$^+$ has a perfect C_{3v} symmetry

with three equivalent B$_5$ pentagons atop the [Ta@B$_{18}$] DR tube. The other C_{3v} B$_4$-[Ta@B$_{18}$]$^+$ structure with three equivalent B$_6$ hexagons atop the B$_{18}$ DR tube turns to be a second-order saddle point on the potential energy surface leading to C_s TS2 and C_s TS3 in e vibrational modes and C_1 TS1 and C_1 TS4 in a$_2$ vibrational mode [20].

Fluxional Bonds in Tubular B$_3$-[Ta@B$_{18}$] (2)

The fluxional behaviors of B$_3$-[Ta@B$_{18}$] and B$_4$-[Ta@B$_{18}$]$^+$ originate from their unique bonding patterns. Molecular orbitals analyses show that both B$_3$-[Ta@B$_{18}$] (2) and B$_4$-[Ta@B$_{18}$]$^+$ (3) possess nine occupied canonical molecular orbitals (CMOs) involving the 6s6p5d hybridized orbitals of the Ta center [20]. Interestingly, as shown in Figure S1–S6, their intermediate states and transition states turn out to follow the 18-electron rule with nine occupied CMOs involving the 6s6p5d hybridized orbitals of the Ta center in slightly different orientations. The nine delocalized CMOs are all well maintained in the fluctuation process in each series. B$_2$-[Ta@B$_{18}$]$^-$ monoanion, [19] B$_3$-[Ta@B$_{18}$] neutral, and B$_4$-[Ta@B$_{18}$]$^+$ monocation therefore all follow the 18-electron rule in the configuration transformation processes on their potential energy surfaces. Such an 18-electron configuration renders high stability to the B$_n$-[Ta@B$_{18}$]^q DR tubular molecular series (n = 2, 3, 4; q = n − 3) in thermodynamics.

As shown in the AdNDP bonding patterns of B$_3$-[Ta@B$_{18}$] (2) depicted in Fig. 3a, B$_3$-[Ta@B$_{18}$] (2) possesses 2 equivalent 2c–2e σ bonds on the V-shaped B–B–B chain with the occupation number of 1.90 |e|, 2 equivalent
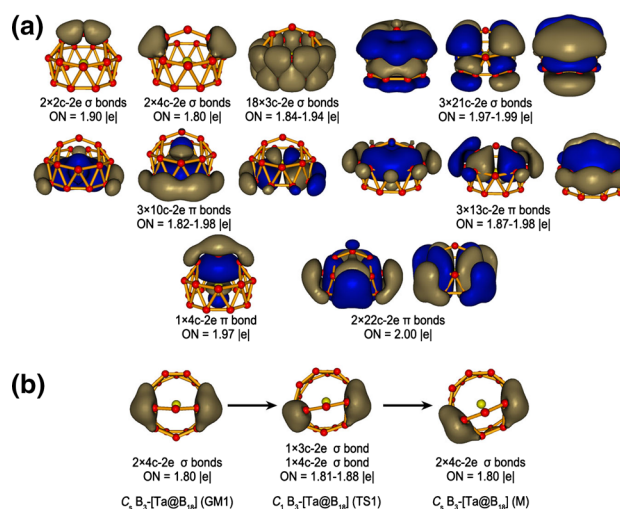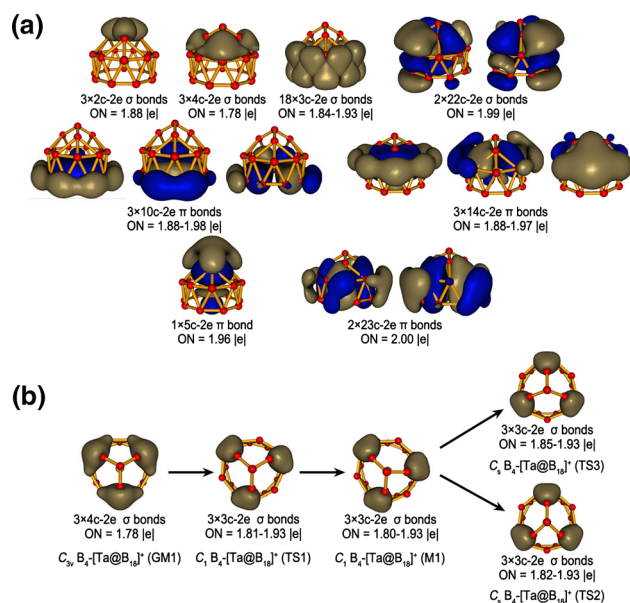

Fig. 3 **a** AdNDP bonding pattern of the global minimum C_s B$_3$-[Ta@B$_{18}$] (2), with the occupation numbers (ONs) indicated. **b** Fluxional 4c–2e and 3c–2e σ bonds atop the Ta-centered [Ta@B$_{18}$] DR tube in global minimum C_s B$_3$-[Ta@B$_{18}$] (GM1), transition state C_1 B$_3$-[Ta@B$_{18}$] (TS1), and intermediate state C_s B$_3$-[Ta@B$_{18}$] (M)

4c–2e σ bonds between the ≡B–B–B≡ chain and the upper B_9 ring atop the [Ta@B_{18}] DR tube with ON = 1.80 |e|, 18 3c–2e σ bonds on the B_{18} tubular unit with ON = 1.84–1.94 |e|, and 3 21c–2e σ bonds involving all the boron atoms in the B_{21} ligand with |ON| = 1.97–1.99 |e|. The remaining 18 valence electrons are distributed in 9 delocalized π bonds involving the 6s6p5d hybridized orbitals of the Ta center, including 3 10c–2e π bonds between Ta center and 9 B atoms at the bottom with ON = 1.82–1.98 |e|, 3 13c–2e π bonds between the Ta center, 3 boron atoms in the B–B–B chain, and 9 boron atoms in the upper B_9 ring with ON = 1.87–1.98 |e|, 1 4c–2e π bond between Ta and the 3 B atoms in the B–B–B chain with ON = 1.97 |e|, and 2 22c–2e π bonds with ON = 2.00 |e| totally delocalized all over the molecule. The Ta center is therefore involved in 9 delocalized π bonds and follows the 18-electron rule, consistent with the CMO analyses discussed above. Interestingly, both the transition state C_1 B_3-[Ta@B_{18}] (TS) (Fig. S7) and intermediate state C_s B_3-[Ta@B_{18}] (M) (Fig. S8) have very similar bonding patterns with C_s GM (Fig. 3a). The major difference occurs in the two σ bonds connecting the B–B–B chain and the B_9 upper ring, with the 2 4c–2e σ bonds in the GM transferred into 1 3c–2e σ bond plus 1 4c–2e σ bond in the transition state (TS1 and TS2) and 2 4c–2e σ bonds in the intermediate state (M) in different orientations (Fig. 3b). There exists thus a 2 4c–2e σ bonds (GM1) → 1 3c–2e σ bond +1 4c–2e σ bond (TS1) → 2 4c–2e σ bonds (M) → 1 3c–2e σ bond + 1 4c–2e σ bond (TS2) → 2 4c–2e σ bonds (GM2) bonding fluctuation in a rotational angle of 40° (Fig. 3b), with 9 equivalent GMs, 9 equivalent intermediates (Ms), and 18 degenerate TSs in a full pseudo-rotational circle.

Fluxional bonds in tubular Ta@B_{22}^+ (3)

The fluxional behaviors of B_4-[Ta@B_{18}]$^+$ (3) are more complicated. As shown in Fig. 4a, it possesses 3 equivalent 2c–2e σ bonds on the B_4 tetrahedron on the top, 3 equivalent 4c–2e σ bonds connecting the B_4 tetrahedron and the upper B_9 ring, 18 3c–2e σ bonds on the B_{18} DR tube, and 2 totally delocalized 22c–2e σ bonds on the whole B_{22} ligand. The remaining 18 valence electrons occupy 9 delocalized π bonds involving the Ta center, including 3 10c–2e π bonds at the bottom, 3 14c–2e π bonds on the top, 1 5c–2e π bond between Ta and the 4 B atoms in the B_4 pyramid, and 2 completely delocalized 23c–2e π bonds over the whole molecule. We notice that the transition states (TS1, TS2, TS3, and TS4) and intermediate states (M1 and M2) all appear to have similar bonding patterns with that of the GM (Figure S9–S12), except the three 4c–2e or 3c–2e σ bonds bridging the B_4 tetrahedron and the upper B_9 ring (Fig. 4b). Specifically, the 3 4c–2e in C_{3v}

Fig. 4 **a** AdNDP bonding pattern of the global minimum C_{3v} Ta@B_{22}^+ (3). **b** Fluxional bonds atop the [Ta@B_{18}] DR tube in global minimum C_{3v} B_4-[Ta@B_{18}]$^+$ (GM1), transition state C_1 B_4-[Ta@B_{18}]$^+$ (TS1), intermediate state C_1 B_4-[Ta@B_{18}]$^+$ (M1), and transition states C_s B_4-[Ta@B_{18}]$^+$ (TS2) and C_s B_4-[Ta@B_{18}]$^+$ (TS3)

GM are transferred into 3 3c–2e σ bonds in C_1 TS1, 3 3c–2e σ bonds in C_1 M1, 3 3c–2e σ bonds in C_1 TS2, and 3 3c–2e σ bonds in C_1 TS3 in different orientations, respectively (Fig. 4b). There exists thus a 3 4c–2e (GM1) → 3 3c–2e (TS1) → 3 3c–2e (M1) → 3 3c–2e (TS2 or TS3) → 3 3c–2e (M2) → 3 3c–2e (TS4) → 3 4c–2e (GM2) bonding fluctuation in each rotational step (40°). 9 equivalent GMs, 18 equivalent intermediates, and 36 transition states are involved in a full pseudo-rotation process.

Fluxional behaviors of the B_n-[Ta@B_{18}]^q complex series (q = n − 3)

There exist obvious similarities and differences between the fluxional behaviors of B_3-[Ta@B_{18}] (2) and B_4-[Ta@B_{18}]$^+$ (3) and that of the previously reported B_2-[Ta@B_{18}]$^-$ (1) [19, 21] (Figs. 1 and 2). First, these B_n-[Ta@B_{18}]^q DR tubular molecular rotors (n = 2, 3, 4; q = n − 3) all contain a B_n unit (n = 2, 3, 4) atop a Ta-centered [Ta@B_{18}] DR tube in their global minima, intermediate states, and transition states. These species in different charge states all follow the 18-electron rule as the size of the B_n unit increases, forming an 18-electron tubular B_n-[Ta@B_{18}]^q series (n = 2, 3, 4; q = n − 3). Such molecular rotors may rotate in a universal direction in an external laser field. Second, they all possess the rotational angle of 40° in a fluxional step due to the existence of the B_9 upper ring in the [Ta@B_{18}] DR tube, with their potential energy

surfaces becoming more and more complicated with the increasing size of the B_n unit. In a rotational step of 40°, B_2-[Ta@B_{18}]$^-$ (**1**) goes through one C_s TS, B_3-[Ta@B_{18}] (**2**) goes through two degenerate C_1 TSs and one C_s intermediate state, while B_4-[Ta@B_{18}]$^+$ (**3**) goes through three TSs (two degenerate C_1 TSs and one C_s TS) and two degenerate C_1 intermediate states. Third, they all possess fluxional 4c–2e and 3c–2e σ-bonds atop the [Ta@B_{18}] DR tube between the B_n unit (n = 2–4) and B_9 upper ring. It is these fluxional bonds which bridge the two rotational components that facilitate the fluxional behaviors of the B_n-[Ta@B_{18}]^q molecular rotors. Finally, the conversion energy barriers of these molecular rotors are not overwhelming, with B_2-[Ta@B_{18}]$^-$ (**1**), B_3-[Ta@B_{18}] (**2**), and [Ta@B_{18}]$^+$ (**3**) possessing the ΔE_a values of 1.59, 4.19, and 1.32 kcal/mol at PBE0 level, respectively. These molecular rotors exhibit almost barrier-free pseudo-rotations which are facilitated by the fluxional 4c–2e and 3c–2e σ-bonds at finite temperatures (Videos S1, S2, and S3 in ESI).

Conclusions

Detailed bonding analyses show the existence of fluxional 4c–2e and 3c–2e bonds in the theoretically predicted B_3-[Ta@B_{18}] (**2**) and B_4-[Ta@B_{18}]$^+$ (**3**), revealing the fluxional bonding nature of the B_n-[Ta@B_{18}]^q complex series (n = 2–4, q = n − 3), similar to the situation in the previously reported B_2-[Ta@B_{18}]$^-$ (**1**) [21]. The high-symmetry C_{3v} B_4-[Ta@B_{18}]$^+$ (**3**) monocation with low energy barriers may serve as a good candidate for infrared photodissociation (IR-PD) spectral measurements in gas phase [15], while B_3-[Ta@B_{18}] (**2**) may be synthesized in neutral solids for high-resolution structural measurements. Fluxional bonds may exist as a general phenomenon with wide applications in chemistry. Investigations on fluxional bonds involved in rapid Cope rearrangements in $C_{10}H_{10}$ and its analogues C_8H_8, C_9H_{10}, and C_8BH_9 [34, 35] are currently underway.

Compliance with Ethical Standards

Conflict of interest All the authors of this paper have no conflict of interest.

References

1. F. A. Cotton, G. Wilkinson, C. A. Murrillo, and M. Bochmann *Advanced Inorganic Chemistry*, 6th ed (Wiley, New York, 1999).
2. L. S. Wang (2016). *Int. Rev. Phys. Chem.* **35**, 69.
3. W. L. Li, X. Chen, T. Jian, T. T. Chen, J. Li, and L. S. Wang (2017). *Nat. Rev. Chem.* **1**, 0071.
4. H. J. Zhai, B. Kiran, J. Li, and L. S. Wang (2003). *Nat. Mater.* **2**, 827.
5. W. Huang, A. P. Sergeeva, H. J. Zhai, B. B. Averkiev, L. S. Wang, and A. I. Boldyrev (2010). *Nat. Chem.* **2**, 202.
6. H. J. Zhai, Y. F. Zhao, W. L. Li, Q. Chen, H. Bai, H. S. Hu, Z. A. Piazza, W. J. Tian, H. G. Lu, Y. B. Wu, Y. W. Mu, G. F. Wei, Z. P. Liu, J. Li, S. D. Li, and L. S. Wang (2014). *Nat. Chem.* **6**, 727.
7. Q. Chen, W. L. Li, Y. F. Zhao, S. Y. Zhang, H. S. Hu, H. Bai, H. R. Li, W. J. Tian, H. G. Lu, H. J. Zhai, S. D. Li, J. Li, and L. S. Wang (2015). *ACS Nano* **9**, 754.
8. Y. J. Wang, Y. F. Zhao, W. L. Li, T. Jian, Q. Chen, X. R. You, T. Ou, X. Y. Zhao, H. J. Zhai, S. D. Li, J. Li, and L. S. Wang (2016). *J. Chem. Phys.* **144**, 064307.
9. Q. Chen, T. T. Chen, H. R. Li, X. Y. Zhao, W. J. Chen, H. J. Zhai, S. D. Li, and L. S. Wang (2019). *Nanoscale* **11**, 9698.
10. W. J. Tian, Q. Chen, H. R. Li, M. Yan, Y. W. Mu, H. G. Lu, H. J. Zhai, and S. D. Li (2016). *Phys. Chem. Chem. Phys.* **18**, 9922.
11. Q. Chen, H. R. Li, W. J. Tian, H. G. Lu, H. J. Zhai, and S. D. Li (2016). *Phys. Chem. Chem. Phys.* **18**, 14186.
12. Q. Chen, H. R. Li, C. Q. Miao, Y. J. Wang, H. G. Lu, Y. W. Mu, G. M. Ren, H. J. Zhai, and S. D. Li (2016). *Phys. Chem. Chem. Phys.* **18**, 11610.
13. Q. Chen, S. Y. Zhang, H. Bai, W. J. Tian, T. Gao, H. R. Li, C. Q. Miao, Y. W. Mu, H. G. Lu, H. J. Zhai, and S. D. Li (2015). *Angew. Chem. Int. Ed.* **54**, 8160.
14. E. Oger, N. R. Crawford, R. Kelting, P. Weis, M. M. Kappes, and R. Ahlrichs (2007). *Angew. Chem. Int. Ed.* **46**, 8503.
15. M. R. Fagiani, X. W. Song, P. Petkov, S. Debnath, S. Gewinner, W. Schöllkopf, T. Heine, A. Fielicke, and K. R. Asmis (2017). *Angew. Chem. Int. Ed.* **56**, 501.
16. I. A. Popov, T. Jian, G. V. Lopez, A. I. Boldyrev, and L. S. Wang (2015). *Nat. Commun.* **6**, 8654.
17. T. Jian, W. L. Li, I. A. Popov, G. V. Lopez, X. Chen, A. I. Boldyrev, J. Li, and L. S. Wang (2016). *J. Chem. Phys.* **144**, 154310.
18. T. Jian, W. L. Li, X. Chen, T. T. Chen, G. V. Lopez, J. Li, and L. S. Wang (2016). *Chem. Sci.* **7**, 7020.
19. W. L. Li, T. Jian, X. Chen, H. R. Li, T. T. Chen, X. M. Luo, S. D. Li, J. Li, and L. S. Wang (2017). *Chem. Commun.* **53**, 1587.
20. H. R. Li, H. Liu, X. X. Tian, W. Y. Zan, Y. W. Mu, H. G. Lu, J. Li, Y. K. Wang, and S. D. Li (2017). *Phys. Chem. Chem. Phys.* **19**, 27025.
21. M. Yan, H. R. Li, X. Y. Zhao, X. Q. Lu, Y. W. Mu, H. G. Lu, and S. D. Li (2019). *J. Comput. Chem.* **40**, 966.
22. M. Yan, H. R. Li, X. X. Tian, Y. W. Mu, H. G. Lu, and S. D. Li (2019). *J. Comput. Chem.* **40**, 1227.
23. X. Y. Zhao, X. M. Luo, X. X. Tian, H. G. Lu, and S. D. Li (2019). *J. Clust. Sci.* **30**, 115.
24. Y. J. Wang, X. Y. Zhao, Q. Chen, H. J. Zhai, and S. D. Li (2015). *Nanoscale* **7**, 16054.
25. G. Martĺnez-Guajardo, A. P. Sergeeva, A. I. Boldyrev, T. Heine, J. M. Ugalde, and G. Merino (2011). *Chem. Commun.* **47**, 6242.
26. Y. J. Wang, X. R. You, Q. Chen, L. Y. Feng, K. Wang, T. Ou, X. Y. Zhao, H. J. Zhai, and S. D. Li (2016). *Phys. Chem. Chem. Phys.* **18**, 15774.
27. Y. G. Yang, D. M. Jia, Y. J. Wang, H. J. Zhai, Y. Man, and S. D. Li (2017). *Nanoscale* **9**, 1443.

28. C. Adamo and V. Barone (1999). *J. Chem. Phys.* **110**, 6158.

29. M. J. Frisch, et al. *Gaussian 09, Revision D.01* (Gaussian Inc., Wallingford, 2013).

30. R. Krishnan, J. S. Binkley, R. Seeger, and J. A. Pople (1980). *J. Chem. Phys.* **72**, 650.

31. D. Feller (1996). *J. Comput. Chem.* **17**, 1571.

32. K. L. Schuchardt, B. T. Didier, T. Elsethagen, L. S. Sun, and V. Gurumoorthi (2007). *J. Chem. Inf. Model.* **47**, 1045.

33. D. Y. Zubarev and A. I. Boldyrev (2008). *Phys. Chem. Chem. Phys.* **10**, 5207.

34. V. N. Staroverov and E. R. Davidson (2000). *J. Am. Chem. Soc.* **122**, 7377.

35. S. G. Semenov and M. V. Makarova (2012). *Russ. J. Gen. Chem.* **82**, 1527.